Catalysis Surveys from Asia, Vol. 9, No. 3, September 2005 (© 2005)
DOI: 10.1007/s10563-005-7552-1

Nanosized CeO_2–SiO_2, CeO_2–TiO_2, and CeO_2–ZrO_2 mixed oxides: influence of supporting oxide on thermal stability and oxygen storage properties of ceria

Benjaram M. Reddy* and Ataullah Khan

Inorganic and Physical Chemistry Division, Indian Institute of Chemical Technology, 500 007, Hyderabad, India

The influence of SiO_2, TiO_2, and ZrO_2 on the structural and redox properties of CeO_2 were systematically investigated by various techniques namely, X-ray diffraction (XRD), Raman spectroscopy (RS), UV–Vis diffuse reflectance spectroscopy (DRS), X-ray photoelectron spectroscopy (XPS), high-resolution transmission electron microscopy (HREM), BET surface area, and thermogravimetry methods. The effect of supporting oxides on the crystal modification of ceria was also mainly focused. The investigated oxides were obtained by soft chemical routes with ultrahigh dilute solutions and were subjected to thermal treatments from 773 to 1073 K. The XRD results suggest that the CeO_2–SiO_2 sample primarily consists of nanocrystalline CeO_2 on the amorphous SiO_2 surface. Both crystalline CeO_2 and TiO_2-anatase phases were noted in the case of CeO_2–TiO_2 sample. Formation of cubic $Ce_{0.75}Zr_{0.25}O_2$ and $Ce_{0.6}Zr_{0.4}O_2$ (at 1073 K) were observed in the case of CeO_2–ZrO_2 sample. The cell 'a' parameter estimations revealed an expansion of the ceria lattice in the case of CeO_2–TiO_2, while a contraction is noted in the case of CeO_2–ZrO_2. The DRS studies suggest that the supporting oxides significantly influence the band gap energy of CeO_2. Raman measurements disclose the presence of oxygen vacancies, lattice defects, and displacement of oxide ions from their normal lattice positions in the case of CeO_2–TiO_2 and CeO_2–ZrO_2 samples. The XPS studies revealed the presence of silica, titania, and zirconia in their highest oxidation states, Si(IV), Ti(IV), and Zr(IV) at the surface of the materials. Cerium is present in both Ce^{4+} and Ce^{3+} oxidation states. The HREM results reveal well-dispersed CeO_2 nanocrystals over the amorphous SiO_2 matrix in the case of CeO_2–SiO_2, isolated CeO_2 and TiO_2 (A) nanocrystals and some overlapping regions in the case of CeO_2–TiO_2, and nanosized CeO_2 and Ce–Zr oxides in the case of CeO_2–ZrO_2 sample. The exact structural features of these crystals as determined by digital diffraction analysis of HREM experimental images reveal that the CeO_2 is mainly in cubic fluorite geometry. The oxygen storage capacity (OSC) as determined by thermogravimetry reveals that the OSC of mixed oxides is more than that of pure CeO_2 and the CeO_2–ZrO_2 exhibits highest OSC.

KEY WORDS: ceria; ceria–silica; ceria–titania; ceria–zirconia; fluorite structure; oxygen storage capacity; XRD; Raman; DRS; XPS; HREM.

1. Introduction

Ceria (CeO_2) is an interesting oxide with unique properties namely its ability to shift easily between reduced and oxidized states ($Ce^{3+} \leftrightarrow Ce^{4+}$) and to accommodate variable levels of bulk and surface oxygen vacancies. These characteristics make it suitable for use as a support as well as catalyst in processes wherein reaction conditions fluctuate between oxidizing and reducing environments [1–3]. Ceria plays multiple roles in various catalyst systems and it is believed that CeO_2 promotes noble metal dispersion, increases thermal stability of Al_2O_3 support, promotes water gas shift (WGS) and steam reforming reactions, favors catalytic activity at the interfacial metal-support sites, promotes CO removal through oxidation by employing its lattice oxygen, stores and releases oxygen (OSC) under lean and rich conditions, and so on [4]. Therefore, CeO_2 containing materials have been receiving a great deal of attention in recent years due to their extensive use in very broad fields, ranging from catalysis [1–7] to ceramics [8], fuel cell technologies [9–11], gas sensors [12,13], solid state electrolytes [14], chromatographic materials [15], cosmetics, etc [16,17]. The technological applicability of CeO_2-containing materials is expanding very rapidly.

As mentioned, the success of ceria in diverse applications is mainly due to its unique combination of an elevated oxygen transport capacity coupled with the ability to shift easily between reduced and oxidized states [1–3,18]. Despite its widespread applications, the use of pure cerium dioxide is highly discouraged because it is poorly thermostable as it undergoes sintering at high temperatures thereby loosing its crucial oxygen storage and release characteristics [3,18,19]. In order to increase its temperature stability and ability to store and release oxygen during operations, other transition and non-transition metal ions could be introduced into the ceria cubic structure [2,3,18–21]. Of course, the redox and catalytic properties of CeO_2 are strongly influenced when it is combined with other transition metals or

* To whom correspondence should be addressed.
E-mail: bmreddy@iict.res.in, mreddyb@yahoo.com

rare-earth oxides [19,22]. In view of their significance much effort has been directed in recent years to find catalyst formulations which can enhance the thermal (textural) stability of ceria without diminishing its special features, such as its unique redox properties and high oxygen mobility.

The redox and catalytic properties of ceria and its composite oxides are primarily dependent upon various factors such as particle size, phase modification, structural defects/distortion (lattice), and chemical non-stoichiometry. In general, reducing the particle size of a catalyst results in increasing surface area and changing its morphology, thus providing a larger number of more reactive edge sites. Especially when the particle size is decreased below 100 nm, the materials become nanophasic where the density of defects increases so that up to half (50%) of the atoms are situated in the cores of defects (grain boundaries, inter phase boundaries, dislocations, etc.). The high density of defects in nanophase materials provide a large number of active sites for gas–solid catalysis, while the diffusivity through the nanometer-sized interfacial boundaries promotes fast kinetics of the catalyst activation and reactions [1,23–26]. Thus, there are several advantages for switching over from conventional to nanosized materials.

Inspired by the unique and promising characteristics of ceria-based mixed oxides and solid solutions for various applications, a systematic study was undertaken to understand the nanostructural evolution of CeO_2–SiO_2, CeO_2–TiO_2, and CeO_2–ZrO_2 mixed oxides. Although, the CeO_2–Al_2O_3 combination has been extensively investigated in the literature for the purpose of automotive pollution control [27–34], supports other than alumina have not been thoroughly investigated even though they have many potential applications other than three-way catalysts [21,29,35,36]. Since, SiO_2, TiO_2, and ZrO_2 are extensively employed as supports as well as catalysts for several applications, we undertook the present investigation to stabilize CeO_2 over the surface of these oxides and subjected them to various thermal treatments. These effects were systematically investigated using XRD, Raman, XPS, HREM, and other techniques. The oxygen storage capacity (OSC) was also determined by a thermogravimetry method to understand reactivity properties of these nanocrystalline oxides.

2. Experimental section

2.1. Preparation of samples

Soft chemical routes with ultrahigh dilute solutions were employed to prepare the investigated CeO_2–SiO_2, CeO_2–TiO_2, and CeO_2–ZrO_2 mixed oxides (1:1 mole ratio based on oxides). Requisite quantities of $CeCl_3 \cdot 7H_2O$ (99.0%, Aldrich) and $TiCl_4$ (99.9%, Aldrich) were dissolved separately in excess double-distilled water and mixed together for making CeO_2–TiO_2. To prepare CeO_2–ZrO_2, desired quantities of ammonium cerium(IV) nitrate (Loba Chemie, GR grade) and zirconium(IV) nitrate (Fluka, AR grade) were dissolved separately in double-distilled water and mixed together. To synthesize CeO_2–SiO_2, the requisite quantities of cerium ammonium nitrate (Loba Chemie, GR grade), dissolved in double-distilled water and colloidal silica (40 wt.%, Fluka, AR grade) were mixed together. Dilute aqueous ammonia solution was added gradually drop-wise to the aforementioned mixture solutions, with vigorous stirring, until precipitation was complete (pH = 8.5). The obtained precipitates were filtered off and washed several times with double-distilled water until free from anion impurities. The obtained cakes were oven dried at 393 K for 12 h and finally calcined at 773 K for 5 h. Some portions of the calcined mixed oxides were once again heated at 873, 973, and 1073 K for 5 h. The rate of heating as well cooling was always maintained at 5 K min^{-1}. For the preparation of pure CeO_2 reference oxide, a similar soft chemical route as detailed above was employed with aqueous solution of ammonium cerium(IV) nitrate (Loba Chemie, GR grade) alone.

2.2. Characterization of samples

The DTA-TGA measurements were made on a Mettler Toledo TG-SDTA apparatus. Sample was heated from ambient to 1273 K under nitrogen flow and the heating rate was 10 K min^{-1}. The BET surface areas were obtained by N_2 adsorption on a Micromeritics Gemini 2360 Instrument. Prior to analysis, samples were oven dried at 393 K for 12 h and flushed with Argon gas for 2 h. Powder X-ray diffraction (XRD) patterns were recorded on a Siemens D-5005 diffractometer using nickel-filtered Cu K_α (0.15418 nm) radiation source. The intensity data were collected over a 2θ range of 3–80° with a 0.02° step size and using a counting time of 1s per point. Crystalline phases were identified by comparison with the reference data from ICDD files. The average crystallite size of CeO_2 was estimated with the help of Debye–Scherrer equation using the XRD data of all prominent lines [37]. The cell 'a' parameter values were calculated by standard cubic indexation method using the intensity of the ceria base peak (111) [38,39].

The Raman spectra were recorded on a DILOR XY spectrometer equipped with a liquid N_2 cooled CCD detector at ambient temperature and pressure. The emission line at 514.5 nm from an Ar^+ ion laser (Spectra Physics) was focused on the sample (analyzing spot 1 μm) under microscope. The power of incident beam on the sample was 3 mW and time of acquisition varied according to the intensity of the Raman scattering. The wavenumbers obtained from spectra are accurate to within 2 cm^{-1}. The diffuse reflectance spectra were obtained over the wavelength range

$\lambda = 200$–800 nm using a GBS-Cintra 10e UV–Vis NIR spectrophotometer with integration sphere diffuse reflectance attachment. Samples were diluted in a KBr matrix by pelletization. The obtained spectra were processed with SPECTRAL 1.70 software, consisting of calculation of $F(R_\infty)$ from the absorbance. The edge energy E_g for allowed transitions was determined by finding the intercept of the straight line in the low-energy rise of a plot of $[F(R_\infty)\ h\nu]^2$ against $h\nu$, where $h\nu$ is the incident photon energy [40,41]. The relation between the diffuse reflectance of the sample (R_∞), absorption (K), and scattering (S) coefficients are related by the Schuster–Kubelka–Munk (SKM) remission function [40,41]: $F(R_\infty) = (1-R_\infty)^2/2\ R_\infty = K/S$.

The XPS measurements were performed on a Shimadzu (ESCA 3400) spectrometer by using Mg K_α (1253.6 eV) radiation as the excitation source. Charging of catalyst samples was corrected by setting the binding energy of the adventitious carbon (C 1s) at 284.6 eV [42,43]. The XPS analysis was done at ambient temperature and pressures typically in the order of less than 10^{-6} Pa. Prior to analysis, the samples were out-gassed in a vacuum oven overnight. Quantitative analysis of atomic ratios was accomplished by determining the elemental peak areas, following the Shirley background subtraction by the usual procedures documented in the literature [42,43]. The high-resolution electron microscopy was carried with a JEM 2010 (Cs = 0.5 mm) microscope. The accelerating voltage was 200 kV with LaB_6 emission current, a point resolution of 0.195 nm and a useful limit of EDS LINK-ISIS. An EDX study was conducted using a probe size of 25 nm to analyze grains of the phases and avoided simultaneous analysis of grains of two phases. Samples were sonically dispersed in ethanol and deposited on a holey carbon copper grid before examination.

The potential OSC was examined by oxygen release characteristics of the powders in the temperature range 573–1073 K. The change in the weight of sample was monitored by thermogravimetry (TG) under cyclic heat treatments in flowing nitrogen and dry air. A commercial Netzsch (Luxx, STA, 409 PC, Germany) TG-DTA analyzer was employed for this purpose. The heat cycle consisted of heating the sample to 1073 K in N_2, cooling down to 423 K in dry air, and again heating to 1073 K in N_2 environment. All heating and cooling rates were 5 K min^{-1}. The weight loss of sample during the second heating cycle was used to measure the oxygen release properties (δ). This technique of OSC evaluation is essentially similar to that described previously [44,45].

3. Results and discussion

3.1. Thermogravimetry and surface area analysis

The as synthesized CeO_2, CeO_2–SiO_2, CeO_2–TiO_2, and CeO_2–ZrO_2 samples were subjected to TGA analysis before calcination. The obtained thermograms, between 323 and 1273 K, are shown in figure 1. These thermograms, in general, reveal one major and two minor weight loss peaks. The TG profile of CeO_2–TiO_2 sample is slightly different in the peak maximum temperature regions from other samples. In all cases, the first major low temperature peak in the range 323–463 K is primarily due to the loss of non-dissociative adsorbed water as well as water held on the surface by hydrogen bonding. The second minor weight loss peak could be due to loss of water held in the micropores of the mixed oxide gels. A further loss of water occurs at slightly higher temperatures due to dehydroxylation of the surface. The TG data of pure ceria sample revealed ~18.2% loss of weight in three consecutive steps between 323 and 733 K, above which no substantial weight loss is observed. In the case of CeO_2–SiO_2 sample, the weight loss from 323 to 470 K is ~10% and from 470 to 723 K is 5%. However, the weight loss

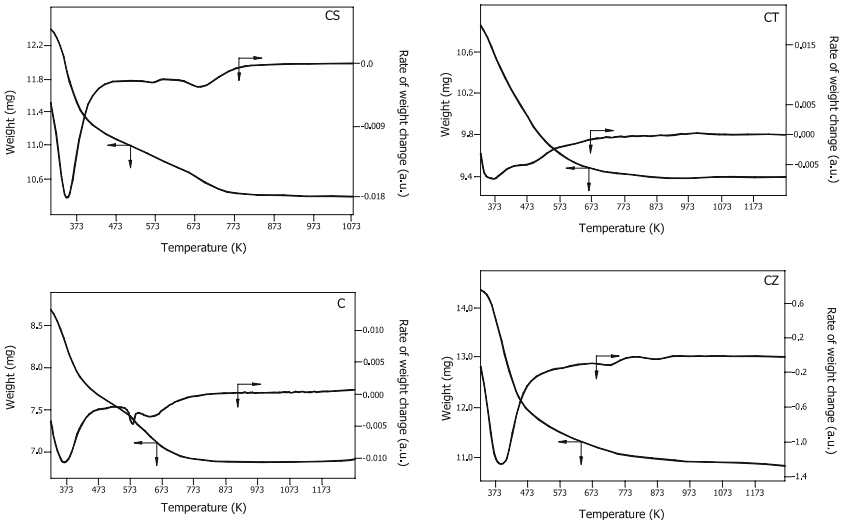

Figure 1. TGA profiles of CeO_2 [C], CeO_2–SiO_2 [CS], CeO_2–TiO_2 [CT], CeO_2–ZrO_2 [CZ] uncalcined samples.

between 723 and 1073 K is only ~1%. It indicates that over the temperature range between 723 and 1073 K, the CeO_2–SiO_2 sample is quite stable in terms of phases and chemical composition. In the case of CeO_2–TiO_2, the loss of weight from 323 to 735 K is ~11% and from 735 to 1273 K is ~0.4%. Thus between 735 and 1273 K, the CeO_2–TiO_2 binary oxide seems to be thermally quite stable. Weight loss of ~23% is observed in the case CeO_2–ZrO_2 sample from 323 to 926 K and thereafter a small loss of 0.6% is observed from 926 to 1273 K.

The N_2 BET surface areas of various samples synthesized in this study and calcined at 773–1073 K are presented in table 1. The 773 K calcined samples exhibit reasonably high specific surface areas. In fact, all samples exhibited much higher surface areas when calcined at 573 K. However, with increasing calcination temperature there is a continuous decrease and the decrease being more after 1073 K calcination. The decrease varied between 48 and 63% depending on the sample under consideration. The observed decrease in the surface area with increasing calcination temperature is a general phenomenon and could be due to various reasons such as better crystallization of the oxides, formation of various mixed oxide phases, and sintering. In particular, the CeO_2–SiO_2 combination showed a high specific surface area among other samples, as it is well known that silica is an effective surface area stabilizer. The efficiency of foreign cations (Si^{4+}, Ti^{4+}, and Zr^{4+}) in preventing the loss of specific surface area at higher temperatures could be related to variations in the rate of crystal growth [46]. The nature and concentration of the foreign cations present in the system govern this variation [19,46].

Table 1
BET surface area, crystallite size, lattice parameter and edge energy measurements of CeO_2, CeO_2–SiO_2, CeO_2–TiO_2 and CeO_2–ZrO_2 samples calcined at different temperatures

Calcination temp. (K)	Surface area ($m^2\ g^{-1}$)	CeO_2 crystallite size[a] (nm)	Lattice parameter(Å)	Edge energy (eV)
CeO_2				
773	41	7.3	5.41	2.94
873	24	10.3	–	–
973	16	20.2	–	–
1073	8	32.5	5.41	2.82
CeO_2–SiO_2				
773	147	3.2	5.41	2.85
873	104	3.6	5.41	–
973	75	4.4	5.40	–
1073	54	6.0	5.40	2.77
CeO_2–TiO_2				
773	59	10.0	5.38	2.88
873	51	10.7	5.38	–
973	42	11.8	5.395	–
1073	31	14.1	5.395	2.96
CeO_2–ZrO_2				
773	84	4.7[b]	5.35	2.70
873	67	4.8[b]	5.33	–
973	51	5.0[b]	5.30	–
1073	36	5.5[b]	5.27	2.80

[a]From XRD.
[b]$Ce_{0.75}Zr_{0.25}O_2$.

3.2. X-ray powder diffraction measurements

The X-ray powder diffraction patterns of various samples investigated in the present study are shown in figure 2. Figure 2a represents the XRD patterns of CeO_2 sample. Formation of a single phase crystalline CeO_2 (PDF-ICDD 34-0394) has been confirmed from the XRD patterns of 773 and 1073 K calcined samples. The ceria–silica mixed oxide (figure 2b) calcined at 773 K exhibits poor crystallinity. Only the broad diffraction lines due to CeO_2 (PDF-ICDD 34-0394) could be seen. With increasing calcination temperature from 773 to 1073 K, a gradual increase in the intensity of the lines due to better crystallization of CeO_2 was noted. Another

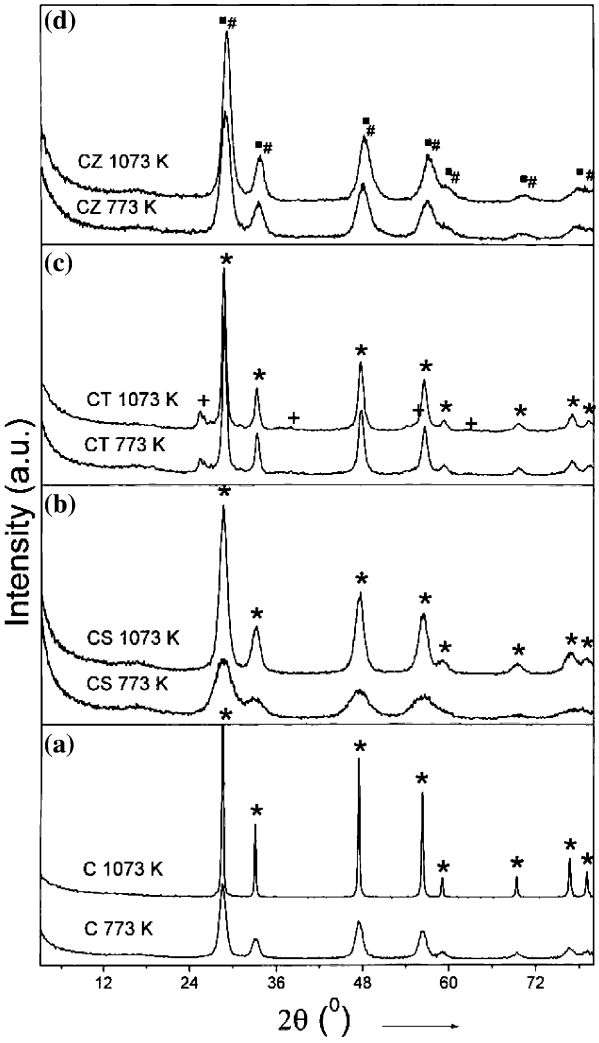

Figure 2. X-ray powder diffraction patterns of CeO_2 [C], CeO_2–SiO_2 [CS], CeO_2–TiO_2 [CT], CeO_2–ZrO_2 [CZ] samples calcined at 773 and 1073 K: (*) Lines due to CeO_2; (■) Lines due to $Ce_{0.75}Zr_{0.25}O_2$; (#) Lines due to $Ce_{0.6}Zr_{0.4}O_2$; (+) Lines due to TiO_2 anatase.

observation to be mentioned from XRD measurements is that there are no extra lines due to compounds or mixed phases between ceria and silica. Recently, Rocchini *et al.* [47,48] have investigated the ceria–silica combination (coprecipitation) and attributed the enhanced textural and thermal stability of these mixed oxides to the formation of an intermediate $Ce_{9.33}(SiO_4)_6O_2$ phase between CeO_2 and SiO_2 which on suitable treatment decomposes into amorphous silica and smaller crystallites of ceria. However, in the present study there was no evidence for the formation of such compound between ceria and silica, which can be attributed to a different preparation method adopted and lower calcination temperatures employed.

The XRD patterns of CeO_2–TiO_2 sample calcined at 773 and 1073 K are shown in figure 2c. These reveal typical diffraction patterns of cubic CeO_2 (PDF-ICDD 34-0394) along with few less intense peaks due to TiO_2-anatase phase (PDF-ICDD 21-1272). With increasing calcination temperature a slight increase in the intensity of the lines due to both these phases could be observed. Recently, Preuss and Gruehn [49] reported various Ce–Ti–O oxides namely, Ce_2TiO_5, $Ce_2Ti_2O_7$, and $Ce_4Ti_9O_{24}$ by heating the appropriate mixtures of solids containing Ce and Ti at 1523 K. However, no such crystalline phases could be observed in the present study. The absence of crystalline Ce–Ti–O compounds may be due to a different preparation method adopted and lower calcination temperatures employed in this investigation. It is an established fact in the literature that transformation of anatase to rutile is thermodynamically feasible beyond 873 K in pure TiO_2 samples [50]. However, there is no evidence regarding the formation of rutile phase even up to 1073 K in the present study. Apparently, the anatase to rutile phase transformation is some how inhibited in the CeO_2–TiO_2 mixed oxide system. As explained by Lin and Yu [51], this phenomenon could be due to stabilization of anatase by the surrounding cerium ions through the formation of Ce–O–Ti bonds. At the interface, titanium atoms are expected to substitute for cerium in the lattice of the cerium oxide to form octahedral Ti sites. The interaction between the tetrahedral Ti and octahedral Ti inhibits the anatase phase transformation to rutile [50]. Anderson and Bard [52] also offered an analogous explanation for TiO_2–SiO_2 mixed oxides where similar inhibition of anatase to rutile phase transformation was observed. It is a well-established fact in the literature that during thermal treatments a progressive depletion of oxygen takes place from the ceria lattice leading to the formation of sub-stoichiometric fluorite structured CeO_{2-x}. Daushter *et al.* [53] in their study on CeO_2–TiO_2 systems have reported the presence of oxygen vacancies. The observed slight shift in the position of diffraction lines towards lower 2θ values (2θ = 28.75–28.67°) originates from the presence of Ce^{3+} ions in the CeO_2 lattice. Owing to a large difference between the ionic dimensions of Ce^{4+} (0.97 Å) and Ce^{3+} (1.03 Å), the lattice expansion of ceria is expected. This aspect has been elaborated in the next paragraphs.

The XRD patterns of CeO_2–ZrO_2 sample calcined at 773 and 1073 K are shown in figure 2d. As can be noted from this figure, the CeO_2–ZrO_2 calcined at 773 K exhibits poor crystallinity. Only the broad diffraction lines due to cubic fluorite type phase with the composition $Ce_{0.75}Zr_{0.25}O_2$ (PDF-ICDD 28-0271) are visible. With increasing calcination temperature an increase in the intensity of the lines due to better crystallization of this phase could be noted. A slight shift in the peak positions (2θ = 28.90–29.32°) with increasing calcination temperature can also be seen which indicate that along with particle growth some compositional changes are also taking place. A detailed analysis of XRD patterns revealed the formation of $Ce_{0.6}Zr_{0.4}O_2$ phase (PDF-ICDD 38-1439) at higher calcination temperature (1073 K) as elaborated in our earlier publication [22]. This is primarily due to a progressive increase of zirconium content into the ceria unit cell, since the ionic radius of Zr^{4+} (0.84 Å) is smaller than Ce^{4+} (0.97 Å) [3]. Recently, Kenevey *et al.* [46] reported the phase segregation phenomenon, which is considered to be surface energy driven. The solid solutions are normally stable as long as the crystallite size does not exceed a critical size, above which the surface energy contribution to the total energy of the system becomes too small to allow its stabilization thereby leading to the phase segregation [46]. Another observation to be mentioned here is that, within the detection limits of XRD technique, there is no evidence about the presence of t-ZrO_2 or m-ZrO_2 phases.

Crystallite size (D_{XRD}) of CeO_2 in pure CeO_2, CeO_2–SiO_2 and CeO_2–TiO_2 samples, and $Ce_{0.75}Zr_{0.25}O_2$ in CeO_2–ZrO_2, as a function of calcination temperature, are summarized in table 1. As can be noted from table 1, the CeO_2 crystallization depends on both the calcination temperature as well as on the type of foreign cation present. In general, an increase in the crystallite size of CeO_2 is observed with increasing calcination temperature, the increase being more in the case of Ce–Ti samples. The phenomenon of crystallite growth can be explained variously in each and every individual system. The co-precipitation of ceria along with colloidal silica yields smaller crystallites of ceria on the surface of silica, which could coalesce under the impact of calcination thus accounting for an increase in the crystallite size [19]. In the case of Ce–Ti system, cubic ceria structure prevailed along with TiO_2 (A) modification. In particular, the Ce–Ti combination exhibited well-crystallized patterns with bigger crystallites within the realm of cubic modification [19]. The formation of solid solution between Ce and Zr retards the crystallite growth thus paving the way for the formation of thermodynamically more stable phases [22]. It should be remembered that the particle size estimates of Ce/Zr

solid solutions are subject to uncertainties attributed to the compositional nonuniformity. When using Scherrer equation, one assumes that the particle size effects are the only source of peak broadening. However, if compositional nonuniformity occurs in the particles, the particle size will be underestimated [22,46].

Using the most intense (111) line of CeO_2 and $Ce_{0.75}Zr_{0.25}O_2$ patterns, cubic indexation and calculation of unit cell parameters have been carried out [38,39]. The evolution of 'a' cell parameter values as a function of calcination temperature are shown in table 1. In particular, the lattice parameter values were estimated to determine whether the foreign cation enters into the CeO_2 lattice resulting in the formation of a solid solution or remains as a separate phase demarcated by a phase boundary. In the case of CeO_2–SiO_2 system, the 'a' cell parameter values estimated are in well agreement with that of pure CeO_2 (100%) phase [39]. However, a slight decrease in the 'a' cell parameter values can be seen at higher calcination temperatures, which could be attributed due to some incorporation of Si^{4+} (0.42 Å) into the ceria lattice. The CeO_2–SiO_2 binary oxide is characterized by the presence of mostly small crystallites of ceria on the surface of silica. Interestingly, in the case of CeO_2–TiO_2 system, a steady increase in the lattice parameter values with increasing calcination temperature can be observed. This could be due to lattice expansion induced by the formation of oxygen vacancies. Under the impact of calcination treatment or dopant-induced defects, depletion of oxygen takes place leading to the formation of sub-stoichiometric fluorite structured CeO_{2-x}. Consequently, the Ce^{3+} (1.03 Å) ions are formed whose ionic radius is larger than that of Ce^{4+} (0.97 Å) ions. In the case of CeO_2–ZrO_2 samples, there is a steady decrease in the lattice parameter values with increasing calcination temperature. This observation can be attributed to shrinkage of lattice due to the replacement of Ce^{4+} (0.97 Å) ions with smaller cations of Zr^{4+} (0.84 Å), in agreement with Vegard's law [54,55]. The progressive decrease in the lattice parameter values can also be taken as an evidence for incremental enrichment of Zr content into the Ce lattice. On the whole, the lattice parameter values of the currently studied systems are well in the range of 5–6 Å and are in good agreement with earlier reports [40,41]. According to literature, the Zr–O bond length in the cubic ZrO_2 is 2.21 Å, which is much shorter than the Ce–O bond length of 2.36 Å in cubic CeO_2 [56]. Thus, when Zr substitutes for Ce centers in the cubic fluorite lattice, two possibilities can be expected: (i) The Zr atoms may be forced into positions where metal–oxygen bond distances are much larger than those observed in the pure ZrO_2, which in turn leads to an effective reduction in the oxidation state of Zr. (ii) Shrinkage of lattice may take place due to nonequivalent metal–oxygen bond lengths and different bonding positions [56]. Based on the information obtained from 'a' cell parameter estimations and XPS measurements (Zr is in the highest oxidation state, Zr(IV), which will be dealt in the latter paragraphs), it can be inferred that lattice contraction is taking place.

3.3. Raman analysis

The cation order-disorder and lattice distortion can in principle be easily detected by conventional X-ray analysis. However, this technique does not allow accurate detection of distortions of oxygen sublattice and or defects in the structure due to poor sensitivity of the technique to the oxygen atoms in the presence of heavy Ce, Ti, and Zr atoms. Since mobility of oxygen atoms in the lattice is a critical property for most of the applications of these materials, both as ionic/electronic conductors and redox catalysts, a deep insight into these fine structural details is desirable. Raman spectroscopy is a good technique sensitive to both M–O bond arrangement and lattice defects [18]. Factor group analyses for the fluorite structure (space group *Fm*3*m*) have been previously performed and indicate that for the cubic structure only one triply degenerate IR active mode is expected, which split into a transverse optical mode (TO) and a longitudinal optical (LO) mode [57,58]. Also a single Raman active mode (F_{2g}) is anticipated. The Raman spectra of pure CeO_2 and various mixed oxides prepared in this study are shown in figure 3. The Raman spectra of CeO_2 calcined at 773 and 1073 K (figure 3a.) display only one prominent peak at 464 cm^{-1}, due to F_{2g} Raman active mode of the fluorite structure [59,60]. The absence of any other features in these spectra indicates the absence of structural defects or oxygen vacancies in the CeO_2 sample. As shown in figure 3b, the Raman spectrum of CeO_2–SiO_2 calcined at 773 K shows a prominent peak at ~457 cm^{-1} and a weak band at 600 cm^{-1}. The band at ~457 cm^{-1} corresponds to the triply degenerate F_{2g} mode and can be viewed as a symmetric breathing mode of the oxygen atoms around cerium ions [61]. With increasing calcination temperature from 773 to 1073 K, the band at ~457 cm^{-1} has been shifted to ~461 cm^{-1}, sharpened, and become more symmetrical. This could be due to better crystallization of ceria at higher calcination temperatures as observed from XRD measurements. It is a known fact in the literature that intensity of Raman band depends on several factors including grain size and morphology. In general, inhomogeneous strain and phonon confinement are responsible for the broad and asymmetric character of the bands as the particle size gets smaller at lower calcination temperatures [62]. The weak band observed near 600 cm^{-1} corresponds to a non-degenerate LO mode of CeO_2 [61,63]. Normally, this mode should not be observed by Raman spectroscopy but the presence of some defects can involve relaxation of selection rules. In particular, this band has been linked to oxygen vacancies in the CeO_2 lattice [64].

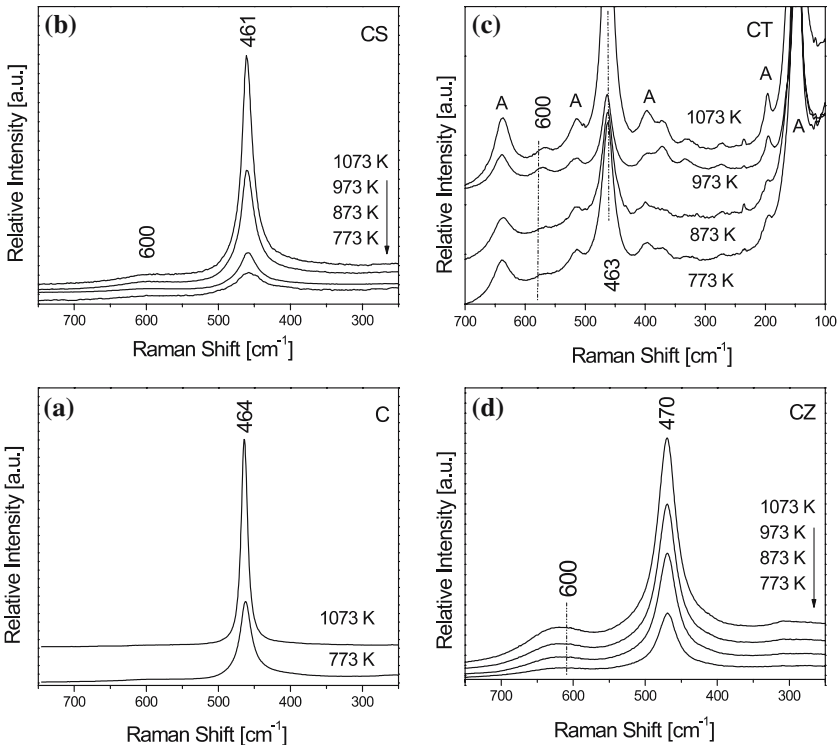

Figure 3. Raman spectra of CeO_2 [C], CeO_2–SiO_2 [CS], CeO_2–TiO_2 [CT], CeO_2–ZrO_2 [CZ] samples calcined at different temperatures.

This peak was observed in the case of nanosized samples and its relative intensity increased as the particle size gets smaller [61]. The same phenomenon is apparent in the present study. For each sample, the spectra were recorded at several points and no shift in the band position or difference of width was noted. This observation reveals clearly that the CeO_2–SiO_2 sample is homogenous. Silica did not show any Raman features, as reported in the literature [65]. This gives an impression that silica forms part of the substrate support on which ceria has been forming a surface overlayer. For very small crystallites (20–200 Å), the lack of long-range order relaxes the momentum conservation selection rule in the Raman scattering process. The Raman line shape in this case will be given by a weighted average of the phonon frequencies extending out into the Brillouin zone, away from $q = 0$ [60]. The result will be a shifted and broadened line shape. The broad band, reflecting the phonon density states is a characteristic of Raman scattering from amorphous materials. Similar observations were made in the present study as expected and could be attributed to the method of preparation adopted. The absence of any other Raman features provides one more inference that silica is not forming any compound with cerium oxide, in line with XRD measurements.

As presented in figure 3c, the Raman spectrum of CeO_2–TiO_2 sample calcined at 773 K shows typical spectra of TiO_2-anatase (space group $I4_1/amd$) [50] and CeO_2. The Raman bands pertaining to anatase phase appear at 147, 196, 397, 514 and 638 cm^{-1}, while ceria exhibits peaks at 272, 463 and 570 cm^{-1}, which are in agreement with the literature reports [61]. McBride *et al.* [64] reported the Raman spectra of $Ce_{1-x}RE_xO_{2-y}$ (RE = Rare Earth) solid solutions and found that the F_{2g} mode becomes asymmetric with the presence of a long low-frequency tail as x increases, and there is also a weak shoulder on the high frequency side of the band, which would evolve into a broad peak at ca. 570 cm^{-1} for a larger x. This broad peak is associated with oxygen vacancies in the solid solutions [62,63]. A similar phenomenon is apparent in the present study, which could be due to the incorporation of Ti^{4+} into the CeO_2 lattice at higher calcination temperatures. However, in agreement with XRD measurements there is no evidence about the formation of detectable compounds between ceria and titania from Raman results. In line with XRD results, there are a few extra broad Raman bands, which could not be assigned to any of the known compounds. The Raman spectrum of CeO_2–ZrO_2 sample (figure 3d) calcined at 773 K is dominated by a strong band at $\sim$470 cm^{-1} and a less prominent broad band at $\sim$600 cm^{-1}. The band at $\sim$470 cm^{-1} can be attributed to the F_{2g} vibration of the fluorite type lattice. The slight shift in the Raman frequency to higher wave numbers could be due to a slight increase in the zirconium content into the ceria–zirconia solid solution as evidenced by XRD results. Thus, Raman results up to certain extent corroborate with the XRD results signifying the enrichment of Zr in the Ce–Zr solid solutions at higher calcination temperatures. No Raman lines due to ZrO_2 could be observed in line with XRD measurements.

According to literature, six Raman active modes ($A_{1g}+3E_g+2B_{1g}$) are expected for t-ZrO_2 (space group $P4_2/nmc$), while for the cubic fluorite structure of CeO_2 (space group $Fm3m$) only one mode is Raman active [58]. As can be noted from figure 3d, the peak at $\sim$470 cm^{-1} becomes sharp with increasing calcination temperature which could be due to better crystallization of ceria–zirconia solid solutions at higher calcination temperatures in line with XRD measurements. It is quite obvious that sintering of the sample at higher calcination temperature increases the intensity of the F_{2g} band. It is also known that sintering of the sample under high temperature conditions leads to the formation of oxygen vacancies, which perturb the local M–O bond symmetry leading to the relaxation of symmetry selection rules. The presence of the broad band near $\sim$600 cm^{-1} is due to LO mode of ceria which arises due to relaxation of symmetry rules as stated earlier [61,63]. In particular, the substitution of zirconium into ceria lattice with an increase in temperature gives rise to oxygen vacancies, which are responsible for the emergence of this band [64]. The appearance of weak bands at $\sim$300 and $\sim$130 cm^{-1} (not shown in figure), at the calcination temperature of 1073 K, can be attributed to displacement of oxygen atoms from their ideal fluorite lattice positions [58].

3.4. UV–Vis DRS measurements

Ceria is n-type semiconductor with band gap energy (E_g) equal to 2.94 eV and consequently it can be activated by irradiation with light in the near UV–Vis range [66]. DRS has been used extensively to study ceria-based materials and transition metal oxides to obtain information on surface co-ordination and different oxidation states of the metal ions by measuring d-d, f-d transitions and oxygen–metal ion charge transfer bands. However, this technique has limitations due to the difficulty in interpreting large bandwidths and specular reflectance often observed in the spectra [40]. The 773 and 1073 K calcined CeO_2, CeO_2–SiO_2, CeO_2–TiO_2, and CeO_2–ZrO_2 samples were investigated by DRS technique. The spectra, in general, were broad and exhibited a myriad of poorly resolved peaks. When compared to pure CeO_2, the mixed oxides exhibit absorption at higher wavelengths. The overall absorption of the mixed oxides is more intense than that of CeO_2. In the spectrum of pure CeO_2, a split absorption was observed at 294 and 336 nm. The former band can be attributed to allowed $O^{2-} \rightarrow Ce^{4+}$ charge transfer transitions [67], while the latter can be assigned to the inter-band transitions which take place in CeO_2 in agreement with previous literature reports [68]. In the 773 K calcined CeO_2–SiO_2 sample, presence of several bands resembling a narrow structure was noticed. These characteristic bands have been reported previously for CeO_2 in a highly dispersed state in SiO_2 matrix and were attributed to localized $O^{2-} \rightarrow Ce^{4+}$ charge transfer transitions involving a number of surface Ce^{4+} ions with different coordination numbers [69–71]. The spectral pattern of the 1073 K calcined sample was very similar to that of the 773 K calcined one, however a slight shift in the band position towards higher wavelengths was observed. The band gap energy (E_g) (table 1) calculations reveal a substantial reduction in the band gap of CeO_2–SiO_2 when compared to CeO_2. A further decrease in the band gap is observed with increasing calcination temperature from 773 to 1073 K. Substitution of Si^{4+} into CeO_2 lattice induces formation of intermediate energy levels in the CeO_2-semiconductor on either side of Fermi level that cause a change in the band gap. In general, the formation of mixed oxide not only alters the charge transfer properties but also influences the crystallinity and optical characteristics of the resultant material. The 773 K calcined CeO_2–TiO_2 sample also exhibited a series of poorly resolved peaks in the range 400–250 nm similar to that of the pure CeO_2 sample. In this case, the 1073 K calcined sample exhibited a shift in the absorption peak maximum towards shorter wavelengths. This shift towards shorter wavelengths is due to the prevailing presence of $Ce^{3+} \leftarrow O^{2-}$ charge transfer transitions along with the existing $Ce^{4+} \leftarrow O^{2-}$ transitions as envisaged earlier [72]. The occurrence of oxygen vacancy defects as noticed from Raman study support the $Ce^{3+} \leftarrow O^{2-}$ transitions in this sample. As shown in table 1, the effective band gap of CeO_2–TiO_2 is lower in comparison to that of TiO_2 (3.2 eV) [50,73]. It is a reported fact in the literature that incorporation of CeO_2 into TiO_2 induces only a small red shift of the electronic absorption with respect to that of pure anatase [74]. The spectrum of 773 K calcined CeO_2–ZrO_2 sample was not well resolved and its absorption band edge exhibited a shift towards longer wavelengths in comparison to pure CeO_2 [73]. Substitution of Zr^{4+} into the CeO_2 lattice and the consequent strain development at the cerium sites, due to lowering of symmetry, causes the observed shift towards higher wavelengths [58]. With increasing calcination temperature the spectrum of 1073 K calcined sample exhibited absorbance towards shorter wavelengths, which could be explained by the predominance of Ce^{4+}-oxygen charge transfers occurring on the low coordination Ce^{4+} ions [69]. The band gap energy estimations (table 1) reveal a substantial decrease for CeO_2–ZrO_2 (773 K) when compared to pure CeO_2 (773 K). Substitution of Zr^{4+} ions into the ceria lattice could be responsible for the apparent decrease in the effective band gap of the semiconductors. The observed increase in the band gap for the 1073 K calcined CeO_2–ZrO_2 sample can be ascribed to occurrence of zirconia rich phases [58]. As per the literature reports, the m-ZrO_2 exhibits two direct inter-band transitions at 5.93 and 5.17 eV, quite different from CeO_2, absorbs light at $\lambda \leq 240$ nm with an absorption threshold edge

near 240 nm [75]. The other t-ZrO_2 phase has a band gap of 5.1 eV and the absorption threshold edge position at 240 nm [76]. In agreement with XRD and Raman measurements, there is no evidence for the presence of m-ZrO_2 and t-ZrO_2 phases from DRS study.

3.5. XPS analysis

In order to understand the nature of interactions between the host cerium ion and the foreign cations, the CeO_2 and various other samples calcined at different temperatures were investigated by XPS technique. The electron binding energies (eV) of O 1s, Si 2p, Ti 2p, Zr 3d, and Ce 3d photoelectron peaks and the corresponding XPS atomic intensity ratios (Ce/Si, Ce/Ti, and Ce/Zr) are presented in table 2. The electron binding energy values agree well with the literature reports [42,43]. The O 1s peak was in general broad and complicated due to non-equivalence of surface oxygen ions. As per the literature, the oxygen ions in pure CeO_2 exhibit intense peaks at 528.6, 528.8, 529.6 and 530.1 eV, respectively [70,77–79]. The O 1s binding energy values reported for various other oxides SiO_2 [70], TiO_2 [43,80], and ZrO_2 [81] are 532.7, 530.0, and 530.6 eV, respectively. The O 1s spectra obtained for various samples were fairly similar, however, signified the presence of modified CeO_2. In the case of CeO_2–SiO_2 sample, the binding energy maximum of the most intense O 1s peak was observed in the range 530.1–530.3 eV which largely signifies the contribution from CeO_2. Judging from the difference in the electronegativity of the CeO_2–SiO_2 system [42,43], the SiO_2 contribution to the overall spectra is negligible, thus supporting the overlayer concept as envisaged earlier [82]. The XPS is a well-known surface technique, with its attenuation depth of few 10–20 Å. As silica forms part of the substrate support its contribution to the overall signal is inadequate. Thus, the XPS results were fairly in agreement with the Raman measurements, giving an impression that ceria over-shadows the silica surface. The O 1s peak of the CeO_2–TiO_2 sample calcined at 773 K showed a binding energy maximum at 530.0 eV owing to the contributions from various oxide species in the sample. The shift of the peak towards higher binding energy and broadening can be attributed to a partial reduction of Ce^{4+} to Ce^{3+} under the conditions of XPS analysis, a well-documented fact in the literature. According to Paparazzo *et al.* [77] sample evacuation under the conditions of XPS analysis leads to partial reduction. The binding energy of the most intense O 1s peak of the CeO_2–ZrO_2 sample was observed at 530.1 eV, which can be attributed to the oxygen atoms bound to $Ce_{0.75}Zr_{0.25}O_2$ solid solution, judging from the difference in the electronegativity of the constituent oxides involved [42,43]. The broadening of the peak and slight increase in the binding energy values, owing to more electronegativity of the zirconium, with increasing calcination temperature can be taken as an evidence for surface enrichment and incorporation of zirconium into the ceria lattice.

Figure 4 displays the Si 2p, Ti 2p, and Zr 3d XP spectra of various mixed oxides investigated in this study. The binding energy of the Si 2p peak (figure 4a), in the case of CeO_2–SiO_2 samples, ranged between 103.6 and 104.0 eV, which agree well with the values reported in the literature [70,82–84]. The poor intensity of the spectra with large peak widths indicates that silica is not

Table 2
XPS core level binding energies of CeO_2, CeO_2–SiO_2, CeO_2–TiO_2, and CeO_2–ZrO_2 samples calcined at different temperatures

Calcination temp (K)	Binding energy (eV)					Atomic ratios Ce/M (Si, Ti & Zr)
	O 1s	Si $2p_{3/2}$	Ti $2p_{3/2}$	Zr $3d_{5/2}$	Ce $3d_{5/2}$	
CeO_2						
773	529.6	–	–	–	884.4	–
1073	530.1	–	–	–	882.9	–
CeO_2–SiO_2						
773	530.1	103.7	–	–	881.7	0.71
873	530.2	103.6	–	–	881.3	0.70
973	530.2	103.8	–	–	881.3	0.71
1073	530.3	103.8	–	–	881.2	0.70
CeO_2–TiO_2						
773	530.0	–	458.7	–	882.0	3.91
873	530.1	–	458.7	–	881.6	2.80
973	530.0	–	458.9	–	881.6	2.24
1073	530.3	–	459.1	–	881.8	1.85
CeO_2–ZrO_2						
773	530.1	–	–	182.2	882.5	2.3
873	530.2	–	–	182.3	881.5	2.1
973	530.3	–	–	182.5	881.5	1.8
1073	530.3	–	–	182.6	881.3	1.6

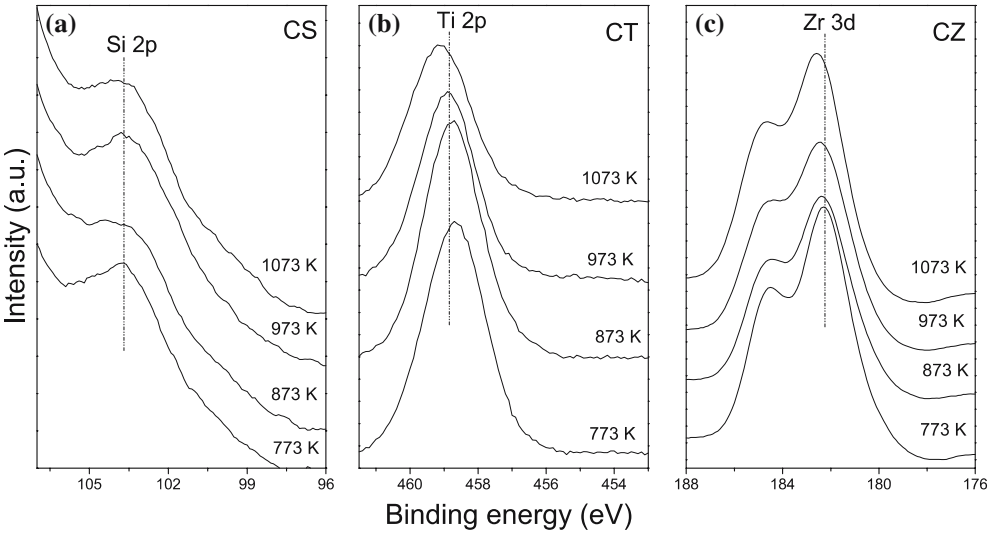

Figure 4. Si 2p, Ti 2p, and Zr 3d XPS spectra of CeO_2–SiO_2 [CS], CeO_2–TiO_2 [CT], CeO_2–ZrO_2 [CZ] samples calcined at different temperatures.

easily accessible at the surface due to the presence of ceria overlayer. The Ti 2p photoemission spectra (figure 4b) of CeO_2–TiO_2 exhibit typical peaks in the range 458.7–459.1 eV for Ti $2p_{3/2}$, which are in agreement with earlier reports [80,85–88]. With increasing calcination temperature broadening of the Ti 2p core-level spectra are observed. The core level spectra of Zr 3d (figure 4c), in the case of CeO_2–ZrO_2, showed progressive broadening along with shift towards higher binding energy from 182.2 to 182.6 eV with increasing calcination temperature indicating the formation of solid solutions between ceria and zirconia in different stoichiometric combinations as envisaged earlier [19,42,43]. The shift towards higher binding energy along with broadening (fwhm 4.1 to 4.3) as a function of calcination temperature signifies the enrichment of Zr and account for the emergence of $Ce_{0.6}Zr_{0.4}O_2$ phase at higher calcination temperatures. The XPS studies indicate that all constituent oxides in the CeO_2–MO_2 (M = Si, Ti, and Zr) mixed oxides are present in their highest oxidation states, Si(IV), Ti(IV) and Zr(IV) and show no sign of reduction under the conditions employed in this study.

The CeO_2 3d photoelectron peaks of various samples investigated in this study are shown in figure 5. The assignment of CeO_2 3d photoelectron peaks is ambiguous due to complex nature of the spectra arising not only because of multiple oxidation states but also due to mixing of Ce 4f levels and O 2p states during the primary photoemission process [70]. This hybridization leads to multiplet splitting of the peaks into doublets, with each doublet showing further structure due to final state effects [89,90]. Based on the works of Burroughs *et al.* [91], Pfau and Schierbaum [79], and Creaser *et al.* [92] the Ce 3d spectrum can be assigned as follows: Two sets of spin-orbital multiplets, corresponding to the $3d_{3/2}$ and $3d_{5/2}$ contributions, are labeled as u and v, respectively. The peaks labeled v and v″ have been assigned to a mixing of Ce $3d^9$ $4f^2$ O $2p^4$ and Ce $3d^9$ $4f^1$ O $2p^5$ Ce(IV) final states, and the peak denoted v‴ corresponds to the Ce $3d^9$ $4f^0$ O $2p^6$ Ce(IV) final state. On the other hand, lines v_0 and v′ are assigned to Ce $3d^9$ $4f^2$ O $2p^5$ and Ce $3d^9$ $4f^1$ O $2p^6$ of Ce(III). The same assignment can be applied to the u structures, which correspond to the Ce $3d_{3/2}$ levels. As displayed in figure 5a the Ce 3d spectra of pure CeO_2 calcined at 773 K exhibits a myriad of peaks due to both Ce^{4+} and Ce^{3+} oxidation states. However, the predominance of Ce^{3+} oxidation-state can be clearly observed from the Ce 3d XP spectra of the 1073 K calcined sample. As shown in figure 5b, the XP spectrum of CeO_2–SiO_2 sample calcined at 773 K exhibits peaks due to the presence of both Ce^{4+} and Ce^{3+}, thus implying that cerium is present at the surface in both 4+ and 3+ oxidation states [82]. With increase in calcination temperature the relative intensity of u′ and v′ annotated peaks increased, indicating an increase in the surface content of Ce^{3+}. Probably the Ce^{3+} has been formed due to the reduction of CeO_2 under the conditions of ultrahigh vacuum treatment during XPS measurements [77,93,94]. However, the presence of Ce_2O_3 was not observed from XRD measurements. As shown in figure 5c, the Ce 3d spectrum of the CeO_2–TiO_2 sample basically denotes a mixture of Ce^{3+}/Ce^{4+} oxidation states giving raise to a myriad of peaks indicating that the surface of the sample is not fully oxidized [85]. With increasing calcination temperature the intensity of the u′/v′ doublet due to primary photoemission from the Ce^{3+} relative to the intensities of the peaks due to photoemission from Ce^{4+} (i.e., u/v, u″/v″ and u‴/v‴) increased gradually up to 873 K and then decreased. An additional peak centered at 880.9 eV was observed in the spectrum [85]. This peak is a shakedown feature resulting from a filled O 2p orbital to a Ce 4f orbital during photoemission from

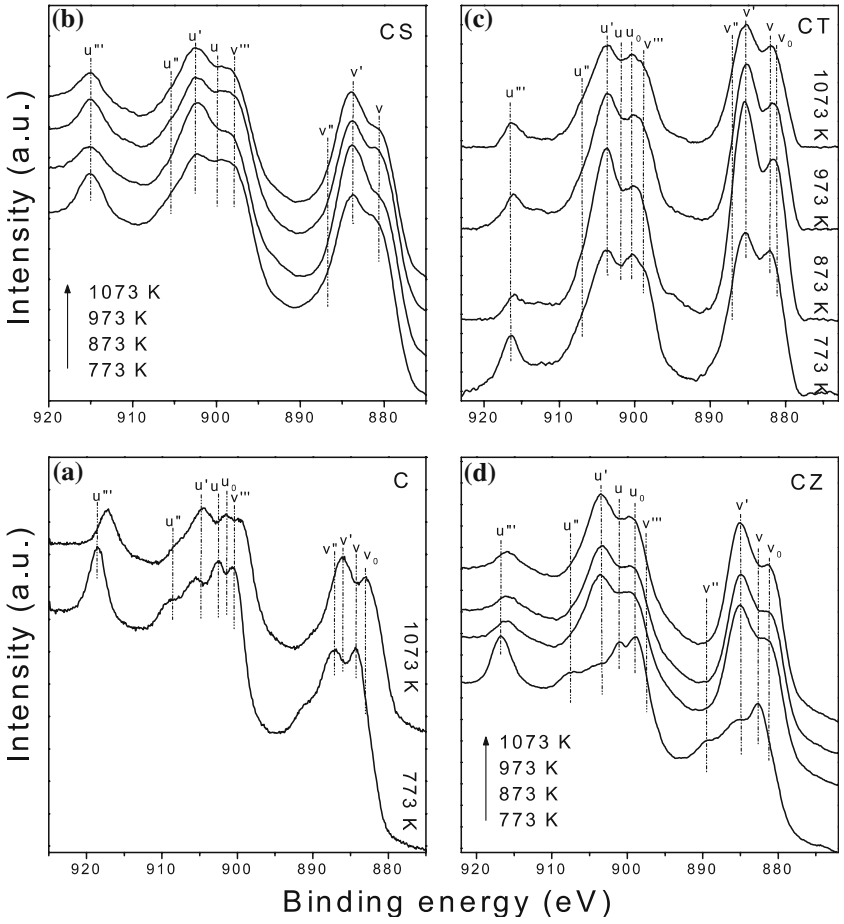

Figure 5. Ce 3d XPS spectra of CeO_2 [C], CeO_2–SiO_2 [CS], CeO_2–TiO_2 [CT], CeO_2–ZrO_2 [CZ] samples calcined at different temperatures.

Ce^{3+} cations. This shakedown feature gives rise to an additional doublet, which is labeled as u_0/v_0 in the spectrum. The presence of u_0/v_0 and u′/v′ doublet peaks indicates that the CeO_2–TiO_2 sample contains some oxygen vacancies and is in partially reduced state. The change in the intensity of the primary photoemission peaks from Ce^{4+} cations (i.e., u/v, u″/v″, and u‴/v‴) with increasing calcination temperature could be due to partial incorporation of Ti^{4+} into the ceria lattice in line with RS measurements. A partial photoreduction of CeO_2 during XPS measurements is also a well-known fact in the literature [77,93,94]. Figure 5d represents the XP spectra of CeO_2–ZrO_2 sample calcined at 773–1073 K. The 773 K calcined sample shows a typical peak shape corresponding to Ce(IV) oxidation state. As the calcination temperature increases, the structures due to v, v″, v‴ and u, u″ disappear progressively and the intensity of the u‴ peak decreases [19]. At higher calcination temperatures the intensity of structures due to u_0, v_0, u′, and v′ increased, indicating an increase in the surface content of Ce(III). As mentioned earlier, the reduction of Ce(IV) under the conditions of ultrahigh vacuum during XPS measurements could lead to the formation of Ce(III).

The Ce/M (M = Si, Ti or Zr) atomic ratios as determined by XPS are presented in table 2. As observed from table 2, the Ce/Si atomic ratios for various CeO_2–SiO_2 samples are fairly constant irrespective of the calcination temperature, thus signifying the fact that ceria crystallites are stabilized over the surface of silica support and the whole system is thermodynamically stable. The Ce/Ti atomic ratios decreased as a function of calcination temperature and the decrease can be attributed to the incorporation of Ti^{4+} cations into the ceria lattice at higher calcination temperatures, thereby increasing the surface content of Ti^{4+} ions, as envisaged earlier by cell parameter estimations [19]. In the case of CeO_2–ZrO_2 sample, the Ce/Zr atomic ratios are found to decrease with increasing calcination temperature, thus supporting the surface enrichment of zirconia due to the formation of zirconium rich $Ce_{0.6}Zr_{0.4}O_2$ phase over the surface. The Ce/M atomic ratios among different systems were found to be far from the theoretical estimations due to the complex nature of the systems envisaged and also the amount of error involved in the XPS quantifications [19,42]. However, the trends observed in a given system (as a function of calcination temperature) provide

valuable information on the surface composition of the sample and fairly support the conclusions drawn from XRD and Raman techniques.

3.6. High-resolution transmission electron microscopy studies

To explore the structural features at atomic level, the HREM studies were performed on some selected representative samples. The TEM global view of the CeO_2–SiO_2 sample calcined at 773 K is shown in figure 6a. A closer inspection of the image reveals the existence of smaller crystals (~3–4 nm) dispersed over an amorphous matrix with different contrasts. For deeper insight, the analyses of high-resolution images were undertaken to establish the structure of the particles [95]. Figure 6b shows the HREM image of the sample subjected to the same thermal treatment. The contrast observed in the experimental image is associated to the face centered cubic structure (fluorite) of the cerium oxide. Well-crystallized CeO_2 grains mixed with SiO_2 (amorphous matrix) are mainly observed [47,96,97]. The presence of bidimensional dark spots can be clearly noted. The digital diffraction pattern (DDP) obtained from the experimental image is also shown as inset in figure 6b. The different spots that are present account for the existence of periodic contrasts in the original experimental micrographs, which correspond to different sets of atomic planes of the crystalline structure. The geometrical arrangements of these reflections are directly related to the structural aspects of the analyzed crystals. Because of this fact the DDPs' are very useful for phase recognition [98,99]. The spots labeled 1, 2, and 3 in the DDP correspond to the interplanar spacings of 3.2, 2.7 and 3.1 Å, respectively, which correspond to the (111), (200) and (1–1–1) planes of ceria in cubic fluorite structure. The energy dispersive X-ray microanalysis (EDX) was also performed to get information on the composition of the surface, which revealed the presence of Ce and Si in stoichiometric proportions. Taking into account the analysis performed on the experimental images, it can be inferred that a good dispersion of the CeO_2 nanophases on the surface of partly amorphous silica matrix has been obtained. This dispersed phase is present in the form of small crystals of 3–4 nm average size.

Figure 7a shows a representative TEM image of the CeO_2–SiO_2 sample calcined at 1073 K. The presence of ceria nanocrystals dispersed over the large silica grains are mainly seen from this image. The dispersed ceria phase seems to be slightly different when compared to that of the sample calcined at 773 K. Also the crystallinity of the sample has increased. In this case, as revealed by the analysis of the subsequent images, the mean size of the CeO_2 crystals increased from 3–4 to a value close to 6–10 nm. The HREM image and the corresponding digital diffraction pattern are depicted in figure 7b. The fringes appeared in the micrograph allow the identification of the crystallographic spacing of the CeO_2 nanocrystallites. In the HREM image, the ceria crystallites can be discriminated as patches of parallel lattice fringes with a distance of ~3.2 Å [CeO_2 (111) lattice planes]. In this image also the bidimensional distribution can be clearly observed. The digital diffraction pattern consists of three diffraction spots labeled 1, 2 and 3 around the undeflected central spot. These represent (111), (200) and (1–1–1) planes of cubic fluorite ceria with 3.1, 2.7 and 3.1 Å interplanar spacings, respectively. The EDX analyses to a greater extent

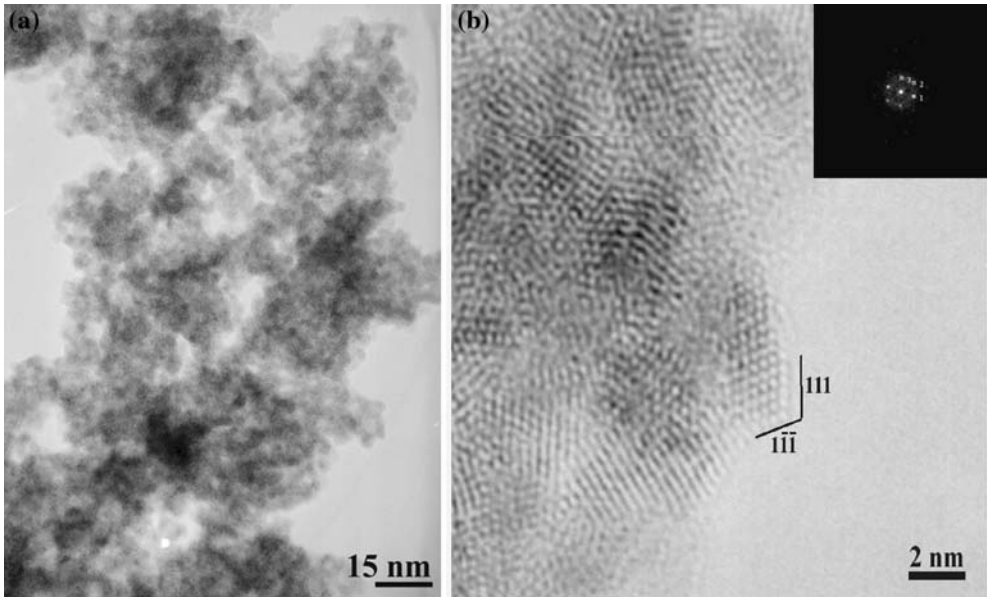

Figure 6. TEM and HREM images of the CeO_2–SiO_2 sample calcined at 773 K. The digital diffraction pattern (DDP) obtained from the corresponding image is also shown.

corroborated with the stoichiometry of the sample. However, in certain areas dispersed ceria phase was completely absent, which indicate the influence of high temperature treatment on the surface segregation of the ceria nanoparticles.

The representative electron micrographs of the CeO_2–TiO_2 sample calcined at 773 and 1073 K are shown in figure 8a and 8b, respectively. The analyses of HREM images of low temperature calcined sample revealed well-crystallized grains of CeO_2 and TiO_2 with approximate grain size of ~20 nm [95]. With increasing calcination temperature the size of ceria grains increased from 20 to ~50 nm while that of titania to ~35 nm. Further, the fringes observed in the micrographs were assigned to the (111) and (101) crystallographic planes of CeO_2 and TiO_2-anatase phases, respectively [95]. The HREM image of the sample calcined at 1073 K shown in figure 9, reveals clearly three distinct regions, the upper top ceria only region, the lower left bottom titania only region, and the intermediate region formed by overlapping of both ceria and titania grains. The corresponding DDPs are also shown as insets in figure 9. Analysis of the spots labeled 1, 2, 3 and 4 (top right inset) revealed the typical diffraction pattern of the anatase-TiO_2, with interplanar spacings of 3.42, 2.66, 3.54 and 2.3 Å corresponding to (101), (110), (01–1) and (–11–2) planes, respectively [100]. The other DDP (left inset) revealed the typical diffraction pattern of CeO_2 phase. The respective interplanar spacings and the corresponding planes for the spots labeled 1, 2, and 3 are as follows: 3.0 Å (111), 2.6 Å (200), and 3.1 Å (1–1–1). The presence of dark and light intermittent bands observed in the micrographs (figure 8a and 8b) could be due to diffraction phenomenon caused by the superimposition of CeO_2 and TiO_2 grains [39]. The EDX analyses revealed the presence of Ce and Ti in appropriate stoichiometries. In particular, the EDX of 1073 K calcined sample confirmed the presence of ceria only, titania only and some overlapping regions in agreement with electron micrographs.

The representative HREM and TEM images of the CeO_2–ZrO_2 sample calcined at 773 and 1073 K are shown in figure 10a and 10b, respectively. Analysis of these and other micrographs (not shown) revealed that the grain size increased from 5 to ~10 nm with increasing calcination temperature from 773 to 1073 K [95]. For deeper insight, analyses of HREM images (figure 10a) and the corresponding digital diffraction patterns were under taken [95]. The DDPs revealed crystals with well-defined bidimensional internal structures. The inter planar spacings 3.0, 2.6 and 3.0 Å measured for the spots labeled 1, 2 and 3 (figure 10a inset) were respectively assigned to (11–1), (200) and (1–11) family planes of the cubic structure, and the geometry of the DDP corresponds to the [011] zone axis. As per the literature reports [39,95,101,102], the fluorite cubic structure normally exhibits only three electron diffraction rings which correspond to the interplanar spacings of ca. 3.1 (111), 2.7 (200), and 1.9 (220) Å. The other two likely phases, tetragonal and monoclinic, exhibit electron diffraction rings at or very close to these cubic spacings, as well as additional spacings. The additional spacings for the tetragonal phase are at 2.1 and possibly at 2.3, 3.7 and 5.3 Å (the last three being possibly active kinetic extinctions) and for the monoclinic at 2.0–2.3, 3.7 and 5.1 Å. These spacings should be treated as approximate since they will vary slightly with the Zr content of the sample. For example, the spots at 5.3 and 5.1 Å would be difficult to separate unambiguously. The absence of any

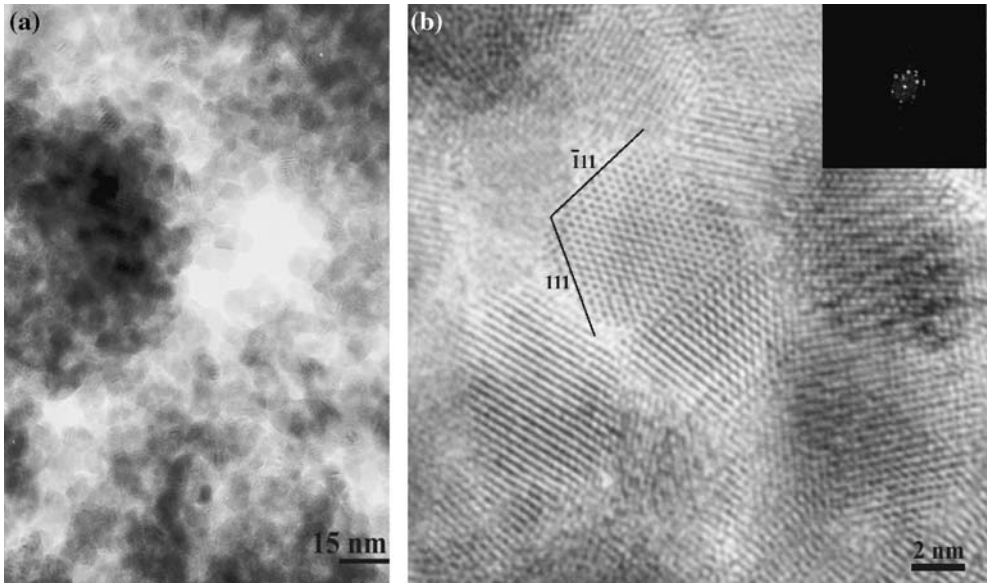

Figure 7. TEM and HREM images of the CeO_2–SiO_2 sample calcined at 1073 K. The digital diffraction pattern (DDP) obtained from the corresponding image is also shown.

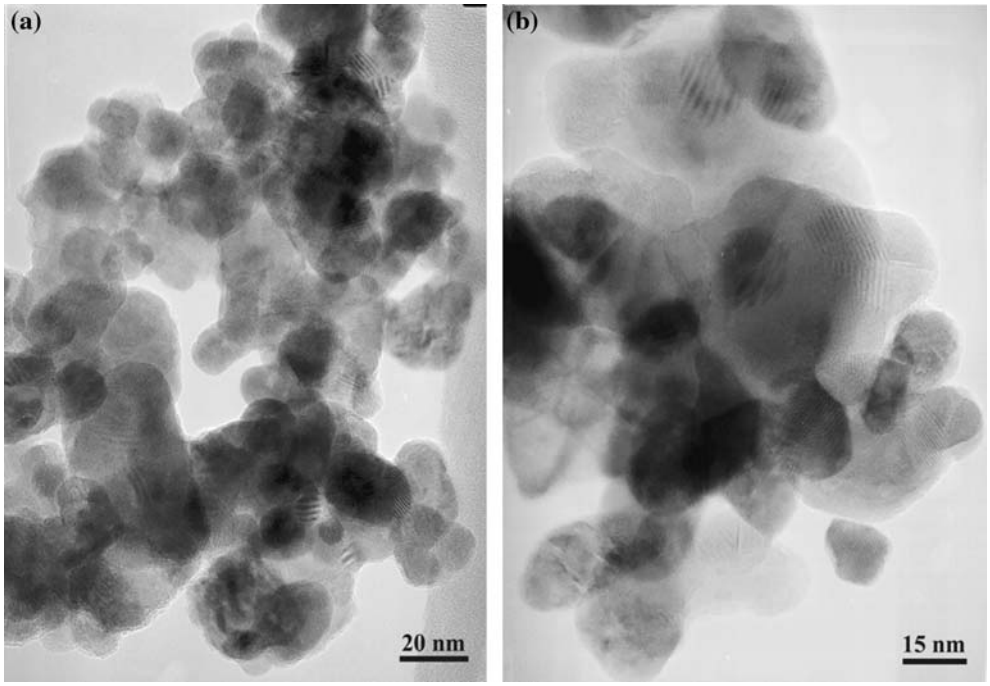

Figure 8. TEM images of CeO_2–TiO_2 sample calcined at (a) 773 K and (b) 1073 K.

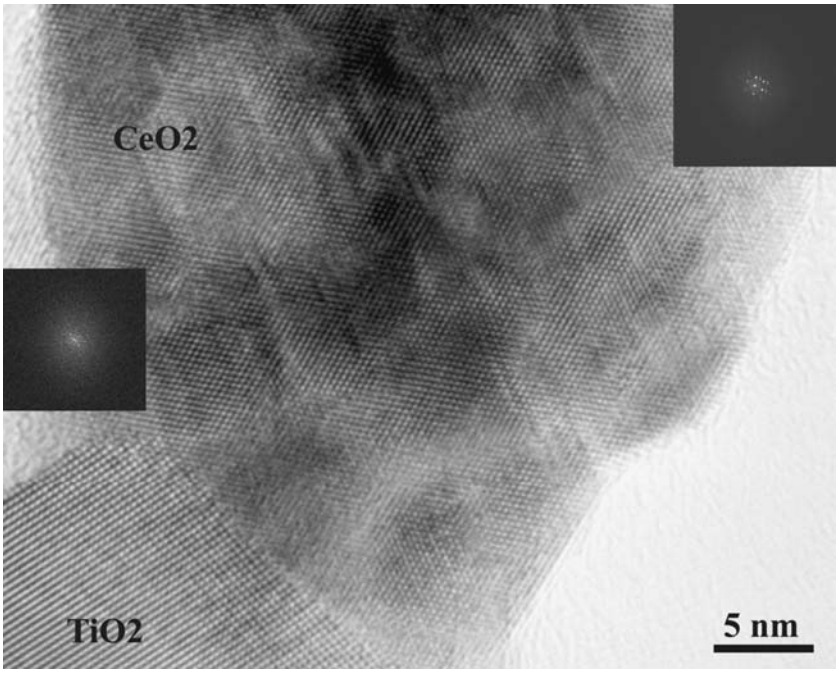

Figure 9. HREM image of CeO_2–TiO_2 sample calcined at 1073 K. The insets in the image are the digital diffraction patterns (DDP) obtained from the corresponding particles.

of these additional spacings clearly indicated that the Ce–Zr oxide system exists in cubic modification [95]. Taking into account the slight contraction of crystal lattice expected by partial substitution of Ce^{4+} ions by smaller Zr^{4+} ions, the simple fluorite type DDPs are quite obvious [19,39]. A significant number of crystals in the present study (figure 10) displayed a pattern of parallel high contrast light and dark bands extending across their surfaces. As per the literature, it may be a diffraction phenomenon caused by the presence of a surface layer of different phase or different crystallographic orientation to that of the supporting crystal [39,101]. On the whole the CeO_2–ZrO_2 sample exhibited patterns of cubic only structures [95].

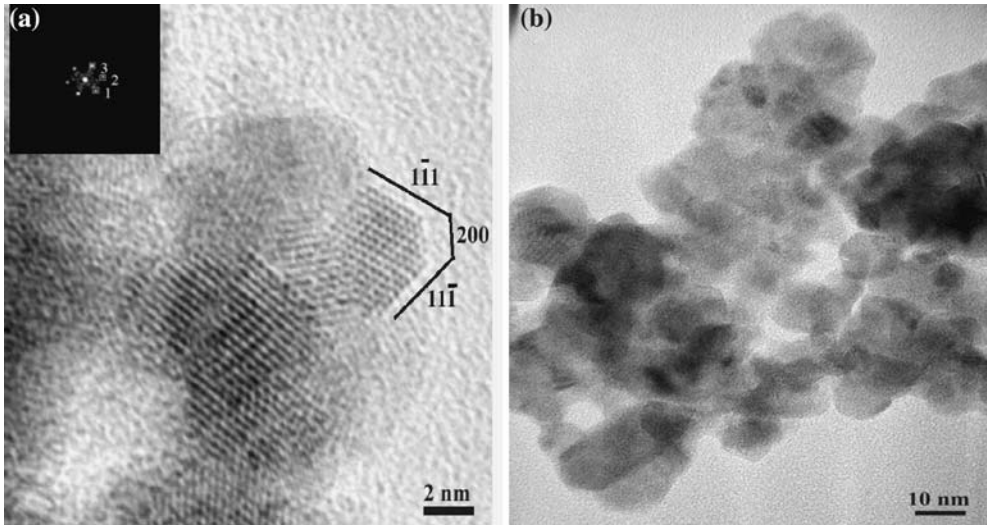

Figure 10. HREM and TEM images of CeO_2–ZrO_2 sample calcined at (a) 773 K and (b) 1073 K, respectively.

3.7. OSC measurements

The potential OSC of mixed oxides and pure CeO_2 (prepared by a similar soft chemical route) were evaluated by thermogravimetry. The percentage weight loss (%) and the corresponding oxygen vacancy concentration or storage capacity (δ) pertaining to various samples are shown in table 3. The parameter 'δ' denotes the number of oxygen vacancies formed in the given sample under the given set of experimental conditions employed. As can be noted from this table, the OSCs of mixed oxide samples are higher than that of pure ceria. The high OSC of CeO_2–SiO_2 compared to CeO_2 could be due to the stabilization of smaller nanocrystals of ceria over the surface of amorphous silica matrix as observed from HREM results. As per literature reports, nanocrystalline ceria has a lower energy of reduction compared to bulk ceria and is responsible for higher defect population [1]. Raman results strongly support this observation. Rocchini *et al.* [48] reported an improvement in the OSC of ceria due to incorporation of small amounts of silica in the mixed ceria–silica composites. In addition, it was proposed that SiO_2 also helps in keeping the ceria crystallites smaller enough to guarantee an elevated oxygen exchange. The CeO_2–TiO_2 system exhibits a slight improvement in the OSC over pure CeO_2. The Raman band observed at 570 cm^{-1} revealed the presence of oxygen vacancy defects in this sample. The presence of oxygen vacancies/Ce^{3+} ions in high proportions could be responsible for the observed high OSC of this mixed oxide. A substantial increase in the OSC for CeO_2–ZrO_2 when compared to CeO_2 and other systems could be noted from table 3. Distortion of O^{2-} sublattice in the mixed oxide permits a higher mobility of the lattice oxygen and reduction is no longer confined to the surface but also extends deep into the bulk [1]. From the structural point of view, there is a quite significant misfit between the ionic radii of Ce^{4+} (0.97 Å) and Zr^{4+} (0.84 Å), which is responsible for modifications of the CeO_2 lattice upon insertion of ZrO_2 [3,19]. Further, the more presence of ZrO_2 in the CeO_2 lattice at higher calcination temperatures makes the lattice more defective, which eventually enhances the mobility of oxygen in the bulk of the CeO_2–ZrO_2 mixed oxides. The relatively intense Raman band observed at ~600 cm^{-1} supports the OSC results. On the whole all mixed oxides exhibit better OSC properties than pure CeO_2 for their eventual catalytic applications [95]. Thus the combined XRD, Raman, UV–Vis DRS, XPS, HREM, and thermogravimetry studies provide valuable information on the physicochemical properties of nanosized CeO_2–SiO_2, CeO_2–TiO_2, and CeO_2–ZrO_2 mixed oxides.

Table 3
Percentage weight loss and corresponding oxygen vacancy concentration, δ, in various samples as determined by thermogravimetry

Sample	Weight loss (%)	δ
CeO_2	0.13	0.04
CeO_2–SiO_2	0.39	0.12
CeO_2–TiO_2	0.26	0.08
CeO_2–ZrO_2	0.52	0.16

4. Conclusions

(1) By adopting soft chemical methodologies, preparation of 1:1 mole ratio CeO_2–SiO_2, CeO_2–TiO_2, and CeO_2–ZrO_2 mixed oxide was undertaken. A pure CeO_2 was also prepared following the same procedure for the purpose of comparison. To evaluate the temperature stability, these oxides were subjected to various thermal treatments from 773 to 1073 K and were examined by using XRD, Raman, UV–Vis DRS, XPS, and HREM

techniques. The effect of support oxides on the crystal structure of ceria was also contemplated. (2) The XRD and HREM studies revealed the presence of CeO_2 nanocrystals over the amorphous SiO_2 matrix in the case of CeO_2–SiO_2 sample, whereas the CeO_2–TiO_2 sample comprised of relatively larger nanocrystals of CeO_2, TiO_2 (A), and some overlapped regions. The formation of cubic $Ce_{0.75}Zr_{0.25}O_2$ and $Ce_{0.6}Zr_{0.4}O_2$ phases were noted in the case of CeO_2–ZrO_2 sample. (3) The measurement of cell parameter 'a' values suggests some incorporation of Si^{4+} into the ceria lattice at higher calcination temperatures, in case of CeO_2–SiO_2 sample. An expansion and contraction of CeO_2 lattice were noted in the case of CeO_2–TiO_2 and CeO_2–ZrO_2 samples, respectively. (4) Raman measurements provided considerable information on the fluorite structure of ceria. In particular, displacement of oxygen sublattice in the fluorite structure and the presence of oxygen vacancies/Ce^{3+} were noted in the case of CeO_2–TiO_2 and CeO_2–ZrO_2 samples. (4) The XPS measurements revealed that the support oxides are in their highest oxidation states, Si^{4+}, Ti^{4+}, and Zr^{4+}. However, cerium displays the presence of both Ce^{4+} and Ce^{3+} oxidation states in different proportions depending on the nature of support oxide and calcination temperature employed. (5) The precise structural features of ceria nanocrystals as determined by digital diffraction analysis of the HREM experimental images revealed that the CeO_2 is mainly in the cubic fluorite geometry. (6) The OSC studies revealed that all these mixed oxides exhibit better redox properties than pure CeO_2. In particular, the CeO_2–ZrO_2 exhibited highest OSC among other combinations.

Acknowledgments

We thank Dr. S. Loridant and Dr. M. Aouine, IRC-Lyon, France, and Dr. Y. Yamada, AIST-Osaka, Japan for providing Raman and HREM, and XPS results, respectively. A.K. is the recipient of senior research fellowship of CSIR, New Delhi. Financial support received from Department of Science and Technology, New Delhi under SERC Scheme (SR/S1/PC-31/2004).

References

[1] A. Trovarelli, *Catalysis by Ceria and Related Materials, Catalytic Science Series*, vol. 2., ed. G.J. Hutchings (Imperial College Press, London, 2002).
[2] A. Trovarelli, Catal. Rev. Sci. Eng. 38 (1996) 439.
[3] A. Trovarelli, C. de Leitenburg and G. Dolcetti, CHEMTECH 27 (1997) 32.
[4] R.D. Monte and J. Kaspar, Catal. Today 100 (2005) 27.
[5] J. Kaspar, P. Fornasiero and M. Graziani, Catal. Today 50 (1999) 285.
[6] J. Kaspar, M. Graziani and P. Fornasiero, in: *Handbook on the Physics and Chemistry of Rare Earths: The Role of Rare-Earths in Catalysis*, vol. 29, K.A. Gschneidner Jr. and L. Eyring (eds.), (Elsevier Science B.V., Amsterdam, 2000), ch. 184, pp. 159–267.
[7] X.M. Song and A. Sayari, Catal. Rev. Sci. Eng. 38 (1996) 329.
[8] M.H. Bocanegra-Bernal and S.D. de la Torre, J. Mater. Sci. 37 (2002) 4947.
[9] B.C.H. Steele, Nature 400 (1999) 619.
[10] J.M. Ralph, A.C. Schoeler and M. Krumpelt, J. Mater. Sci. 36 (2001) 1161.
[11] B.C.H. Steele and A. Heinzel, Nature 414 (2001) 345.
[12] W.C. Maskell, Solid State Ionics 134 (2000) 43.
[13] J.H. Lee, J. Mater. Sci. 38 (2003) 4247.
[14] J.R. Jurado, J. Mater. Sci. 36 (2001) 1133.
[15] R.A. Shalliker and G.K. Douglas, J. Liq. Chromatogr. Relat. Technol. 21 (1998) 2413.
[16] R.X. Li, S. Yabe, M. Yamashita, S. Momose, S. Yoshida and S. T. Yin Sato, Mater. Chem. Phys. 75 (2002) 39.
[17] C. Piconi and G. Maccauro, Biomaterials 20 (1999) 1.
[18] R.D. Monte and J. Kaspar, J. Mater. Chem. 15 (2005) 633.
[19] B.M. Reddy, A. Khan, Y. Yamada, T. Kobayashi, S. Loridant and J.C. Volta, J. Phys. Chem. B 107 (2003) 11475.
[20] W. Liu and M. Flytzani-Stephanopoulos, J. Catal. 153 (1995) 304.
[21] J. Rynkowski, J. Farbotko, R. Touroube and L. Hilaire, Appl. Catal. A: Gen. 121 (1995) 81.
[22] B.M. Reddy, A. Khan, Y. Yamada, T. Kobayashi, S. Loridant and J.C. Volta, Langmuir 19 (2003) 3025.
[23] A. Tschope, J.Y. Ying, in: *Nanophase Materials: Synthesis-Properties-Applications*, G.C. Hadjipanayis and R.W. Siegel (eds.), (Kluwer, London, 1994), p. 781.
[24] Y. Zhang, A. Andersson and M. Muhammed, Appl. Catal. B: Environ. 6 (1995) 325.
[25] P.L. Dai-Boyes, Catal. Rev. Sci. Eng. 34 (1992) 1.
[26] F. Zhang, S.-W. Chan, J.E. Spanier, E. Apak, Q. Jin, R.D. Robinson and I.P. Herman, Appl. Phys. Lett. 80 (2002) 127.
[27] M. Sugiura, Catal. Surveys Asia 7 (2003) 77.
[28] M.H. Yao, R.J. Baird, F.W. Kunz and T.E. Hoost, J. Catal. 166 (1997) 67.
[29] M. Fernández-García, A. Martínez-Arias, A.B. Hungría, A. Iglesias-Juez, J.C. Conesa and J. Soria, Phys. Chem. Chem. Phys. 4 (2002) 2473.
[30] P.W. Park and J.S. Ledford, Langmuir 12 (1996) 1794.
[31] S. Damyanova, C.A. Perez, M. Schmal and J.M.C. Bueno, Appl. Catal. A Gen. 234 (2002) 271.
[32] M.A. Centeno, M. Paulis, M. Montes and J.A. Odriozola, Appl. Catal A: Gen. 234 (2002) 65.
[33] A. Martinez-Arias, M. Fernandez-Garcia, L.N. Salamanca, R.X. Valenzuela, J.C. Conesa and J. Soria, J. Phys. Chem. B 104 (2000) 4038.
[34] M. Ozawa, K. Matuda and S. Suzuki, J. Alloys Compd. 303–304 (2000) 56.
[35] E. Rocchini, A. Trovarelli, J. Llorca, G.W. Graham, W.H. Weber, M. Maciejewski and A. Baiker, J. Catal. 194 (2000) 461.
[36] E. Rocchini, M. Vicario, J. Llorca, C. de Leitenburg, G. Dolcetti and A. Trovarelli, J. Catal. 211 (2002) 407.
[37] H.P. Klug and L.E. Alexander, *X-ray Diffraction Procedures for Polycrystalline and Amorphous Materials* 2 ed. (John Wiley and Sons, New York, 1974).
[38] C. Bozo, F. Gaillard and N. Guilhaume, Appl. Catal. A Gen. 220 (2001) 69.
[39] G. Colon, M. Pijolat, F. Valdivieso, H. Vidal, J. Kaspar, E. Finocchio, M. Daturi, C. Binet, J.C. Lavalley, R.T. Baker and S. Bernal, J. Chem. Soc. Faraday Trans. 94 (1998) 3717.
[40] B.M. Weckhuysen and R.A. Schoonheydt, Catal. Today 49 (1999) 441.
[41] X. Gao and I.E. Wachs, J. Phys. Chem. B 104 (2000) 1261.
[42] D. Briggs and M.P. Seah, (eds.), *Practical Surface Analysis, 2nd edn.; Auger and X - Ray Photoelectron Spectroscopy,* vol. 1 (Wiley, New York, 1990).

[43] C.D. Wagner, W.M. Riggs, L.E. Davis and J.F. Moulder, in: *Handbook of X-Ray Photoelectron Spectroscopy,* G.E. Muilenberg (ed.) (Perkin-Elmer Corporation, Minnesota, 1978).
[44] M. Ozawa and C.K. Loong, Catal. Today 50 (1999) 329.
[45] A.D. Logan and M. Shelef, J. Mater. Res. 9 (1994) 468.
[46] K. Kenevey, F. Valdivieso, M. Soustelle and M. Pijolat, Appl. Catal. B: Environ. 29 (2001) 93.
[47] E. Rocchini, A. Trovarelli, J. Llorca, G.W. Graham, W.H. Weber, M. Maciejewski and A. Baiker, J. Catal. 194 (2000) 461.
[48] E. Rocchini, M. Vicario, J. Llorca, C. de Leitenburg, G. Dolcetti and A. Trovarelli, J. Catal. 211 (2002) 407.
[49] A. Preuss and R. Gruehn, J. Solid State Chem. 110 (1994) 363.
[50] K.I. Hadjiivanov and D.G. Klissurski, Chem. Soc. Rev. 25 (1996) 61.
[51] J. Lin and J.C. Yu, J. Photochem. Photobiol. A: Chem. 116 (1998) 63.
[52] C. Anderson and A.J. Bard, J. Phys. Chem. 98 (1994) 1769.
[53] A. Dauscher, L. Hilaire, F. Le Normand, W. Muller, G. Maire and A. Vasquez, Surf. Interf. Anal. 16 (1990) 341.
[54] M. Yashima, H. Arashi, M. Kakihana and M. Yoshimura, J. Am. Ceram. Soc. 7 (1992) 1541.
[55] R.D. Shannon, Acta Crystallogr., Sect. A: Cryst. Phys. Diffr., Theor. Gen.Crysallogr. 32 (1976) 751.
[56] G. Liu, J.A. Rodriguez, J. Hrbek, J. Dvorak and C.H.F. Peden, J. Phys. Chem. B 105 (2001) 7762.
[57] T. Hirata, E. Asari and M. Kitajima, J. Solid State Chem. 110 (1994) 201.
[58] V.S. Escribano, E.F. Lopez, M. Panizza, C. Resini, J.M.G. Amores and G. Busca, Solid State Sci. 5 (2003) 1369.
[59] A. Martinez-Arias, M. Fernandez-Garcia, L.N. Salamanca, R.X. Valenzuela, J.C. Conesa and J. Soria, J. Phys. Chem. B 104 (2000) 4038.
[60] J.Z. Shyu, W.H. Weber and H.S. Gandhi, Phys. Chem. 92 (1988) 4964.
[61] X.-M. Lin, L.-P. Li, G.-S. Li and W.-H. Su, Mater. Chem. Phys. 69 (2001) 236.
[62] J.E. Spanier, R.D. Robinson, F. Zhang, S.-W. Chan and I.P. Herman, Phys. Rev. B 64 (2001) 245407.
[63] W.H. Weber, K.C. Hass and J.R. McBride, Phys. Rev. B 48 (1993) 178.
[64] J.R. Mc Bride, K.C. Hass, B.D. Poindexter and W.H. Weber, J. Appl. Phys. 76 (1994) 2435.
[65] I.E. Wachs and G. Deo, J. Phys. Chem. 95 (1991) 5889.
[66] K.B. Sundaram and P. Wahid, Phys. Rev. B 161 (1990) K163.
[67] R. Li, S. Yabe, M. Yamashita, S. Momose, S. Yoshida, S. Yin and T. Sato, Mater. Chem. Phys. 75 (2002) 39.
[68] C. Binet, A. Bardi and J.C. Lavalley, J. Phys. Chem. 98 (1994) 6392.
[69] A. Bensalem, J.C. Muller and F. Bozon-Verduraz, J. Chem. Soc. Faraday Trans. 88 (1992) 153.
[70] A. Bensalem, F. Bozon-Verduraz, M. Delamar and G. Bugli, Appl. Catal. A Gen. 121 (1995) 81.
[71] A. Rakai, A. Bensalem, J.C. Muller, D. Tessier and F. Bozon-Verduraz, in: *Proc. 10th Int. Cong. Catal.,* L. Guczi (ed.) (Amsterdam, Elsevier, 1992), p. 1875.
[72] M.I. Zaki, G.A.M. Hussein, S.A.A. Mansour, H.M. Ismail and G.A.H. Mekhemer, Colloids Surf. A 127 (1997) 47.
[73] G.R. Bamwenda, K. Sayama and H. Arakawa, Chem. Lett. 30 (1996) 157.
[74] J.M. Coronado, A.J. Maira, A.M. Arias, J.C. Conesa and J. Soria, J. Photochem. Photobiol A Chem. 150 (2002) 213.
[75] C.R. Aita and C. Kwok, J. Am. Ceram. Soc. 73 (1990) 3209.
[76] M. Scheithauer, R.K. Graselli and H. Knozinger, Langmuir 14 (1998) 3019.
[77] E. Paparazzo, G.M. Ingo and N. Zacchetti, J. Vac. Sci. Technol. A 9 (1991) 1416.
[78] G. Praline, B.E. Koel, R.L. Hance, H.-I. Lee and J.M. White, J. Elect. Spect. Relat. Phenom. 21 (1980) 71.
[79] A. Pfau and K.D. Schierbaum, Surf. Sci. 321 (1994) 71.
[80] J. Biener, M. Baumer, J. Wang and R. Madrix, J. Surf. Sci. 450 (2000) 12.
[81] A. Galtayries, R. Sporken, J. Riga, G. Blanchard and R. Caudano, J. Elec. Spect. Relat. Phenom. 88–91 (1998) 951.
[82] B.M. Reddy, A. Khan, Y. Yamada, T. Kobayashi, S. Loridant and J.C. Volta, J. Phys. Chem. B 106 (2002) 10964.
[83] B.M. Reddy, I. Ganesh and E.P. Reddy, J. Phys. Chem. B 101 (1997) 1769.
[84] V.I. Bukhtiyarov, Catal. Today 56 (2000) 403.
[85] B.M. Reddy, A. Khan, Y. Yamada, T. Kobayashi, S. Loridant and J.C. Volta, J. Phys. Chem. B 107 (2003) 5162.
[86] Q. Wang and R. Madrix, J. Surf. Sci. 474 (2001) L213.
[87] B.M. Reddy, B. Chowdhury, I. Ganesh, E.P. Reddy, T.C. Rojas and A. Fernández, J. Phys. Chem. B 102 (1998) 10176.
[88] B.M. Reddy, I. Ganesh, E.P. Reddy, A. Fernández and P.G. Smirniotis, J. Phys. Chem. B 105 (2001) 6227.
[89] G.S. Wong and J.M. Vohs, Surf. Sci. 498 (2002) 266.
[90] D.R. Mullins, S.H. Overbury and D.R. Huntley, Surf. Sci. 409 (1998) 307.
[91] A. Burroughs, A.F. Hamnett, G. Orchard and G. Thornton, J. Chem. Soc. Dalton Trans. 1 (1976) 1686.
[92] D.A. Creaser, P.G. Harrison, M.A. Morris and B.A. Wolfindale, Catal. Lett. 23 (1994) 13.
[93] P.W. Park and J.S. Ledford, Langmuir 12 (1996) 1794.
[94] J.L.G. Fierro, J. Soria, J. Sanz and J.M. Rojo, J. Solid State Chem. 66 (1987) 154.
[95] B.M. Reddy, A. Khan, P. Lakshmanan, M. Aouine, S. Loridant and J.C. Volta, J. Phys. Chem. B 109 (2005) 3355.
[96] L. Lepinski and M. Wolcyrz, J. Solid State Chem. 131 (1997) 121.
[97] L. Lepinski, M. Wolcyrz and M. Marchewka, J. Solid State Chem. 168 (2002) 110.
[98] C. López-Cartes, J.A. Pérez-Omil, J.M. Pintado, J.J. Calvino, Z.C. Kang and L. Eyring, Ultramicroscopy 80 (1999) 19.
[99] S. Bernal, J.J. Calvino, M.A. Cauqui, J.M. Gatica, C. Lopez-Cartes, J.A. Perez-Omil and J.M. Pintado, Catal. Today 77 (2003) 385.
[100] M.S.P. Francisco, V.R. Mastelaro, P.A.P. Nascente and A.O. Florentino, J. Phys. Chem. B 105 (2001) 10515.
[101] G. Colon, F. Valdivieso, M. Pijolat, R.T. Baker, J.J. Calvino and S. Bernal, Catal. Today 50 (1999) 271.
[102] B.M. Reddy, P. Lakshmanan, A. Khan, C.-L. Cartes, T.C. Rojas and A. Fernández, J. Phys. Chem. B 109 (2005) 1781.